An Earth-Abundant Ni-Based Single-Atom Catalyst for Selective Photodegradation of Pollutants

Gianvito Vilé,* Priti Sharma, Maarten Nachtegaal, Flavio Tollini, Davide Moscatelli, Anna Sroka-Bartnicka, Ondrej Tomanec, Martin Petr, Jan Filip, Izabela S. Pieta, Radek Zbořil, and Manoj B. Gawande*

This article is dedicated to the memory of Professor Maria Flytzani-Stephanopoulos, in remembrance and recognition of her pioneering contributions to the field of single-atom catalysis, and for her support to younger generations.

Highly efficient catalytic technologies are urgently needed to remove pharmaceutical pollutants from water. In this work, the preparation, characterization, and photocatalytic performance of an earth-abundant Ni-based heterogeneous catalyst featuring highly dispersed Ni species over nanosheets of carbon nitride are reported. The absence of any metallic nickel phase has been confirmed by spectrometric analyses, unveiling the Ni—N environment for the metal centers and attaining synergistic interfacial carrier transfer via N—Ni—N coordination. By combining advanced characterizations with kinetic investigations, it is demonstrated that these newly formed isolated single atoms of Ni act as a bridge, facilitating faster electron transfer, increasing the charge density on Ni, and reducing the photocarrier transfer barrier. Compared to literature precedents, this substantially enhances the degradation of gemfibrozil, a model pharmaceutical pollutant found in wastewater, reducing the formation of toxic benzenic byproducts during photooxidation. This effect, which is not observed over conventional nanoparticle-based materials, discriminates the role of single-atom and nanoparticle-based catalysis during degradation of pollutants. This work opens new avenues in designing selective and earth-abundant photocatalysts for advanced oxidation processes, showing the importance of atom coordination to control the surface and catalytic properties of single-atom materials.

1. Introduction

The removal of pharmaceuticals from water is a major scientific and technological challenge among the United Nations Millennium Development Goals.[1] Contaminant photodegradation processes based on the exploitation of nanocatalysts are gaining momentum,[2] and this popularity is linked with the low cost, low toxicity, and unique semiconductive abilities of many novel nanomaterials, which are able to generate hydroxyl radicals (•OH) and oxidize persistent pollutants into biodegradable byproducts with an unprecedented selectivity.[3] This outperforms state-of-the-art TiO_2 catalysts, which often do not ensure a complete contaminant degradation. For example, in the TiO_2/C-assisted photocatalytic oxidation of gemfibrozil, one of the drugs found in wastewater effluents, stable benzene moieties are formed during degradation, and these are released in the "purified" water, creating acute toxicity and causing major environmental issues.[4] For this reason, non-TiO_2-based photocatalysts featuring the use of MoS_2,

Dr. G. Vilé, F. Tollini, Dr. D. Moscatelli
Department of Chemistry, Materials, and Chemical Engineering "Giulio Natta"
Politecnico di Milano
Piazza Leonardo da Vinci 32, 20133 Milan, Italy
E-mail: gianvito.vile@polimi.it

The ORCID identification number(s) for the author(s) of this article can be found under https://doi.org/10.1002/solr.202100176.

Dr. P. Sharma, Dr. O. Tomanec, M. Petr, Dr. J. Filip, Prof. R. Zbořil, Dr. M. B. Gawande
Regional Centre of Advanced Technologies and Materials
Czech Advanced Technology and Research Institute
Palacký University Olomouc
Šlechtitelů 27, 779 00 Olomouc, Czech Republic

Dr. M. Nachtegaal
Paul Scherrer Institute
Forschungsstrasse 111, 5232 Villigen, Switzerland

Prof. A. Sroka-Bartnicka
Faculty of Pharmacy
Medical University of Lublin
Chodzki 4a, 20-093 Lublin, Poland

fullerenes, graphene, N-containing carbons, ZnO, Bi_2WO_6, WS_2, and Ag_3PO_4 are regarded as next-generation solutions for selective photocatalytic degradation of persistent micropollutants.[5] In particular, graphitic carbon nitride (gC_3N_4) is a promising photoactive material only based on earth-abundant elements (i.e., C and N), highly stable from a thermal and chemical viewpoint, and with appropriate bandgap ($\approx$2.7 eV), to enable visible light absorption.[6] However, its photocatalytic activity is limited because of the fast photoinduced electron–hole pair recombination rate, giving rapid charge carrier recombination. Therefore, improving its electronic properties via nanostructural modifications and elemental incorporation is a requirement for carbon nitride samples.

Single-atom catalysts (SACs) are a new class of materials bridging these gaps.[7] These materials, which consist of isolated single metals tenaciously entrapped within the cavities of a porous carrier, represent the optimal utilization of transition metals, offering facile material handling similar to that of the traditional heterogeneous catalysts.[8] Carbon nitride motifs are the most chosen carrier for metal anchoring to prepare SACs.[9] In fact, the polymeric structure of gC_3N_4 is optimal due to its nitrogen-rich pores that can accommodate in a stable manner the metal species through electronic stabilization with the lone N pairs.[10,11] This incorporation of metal species within the carrier pores can effectively enhance the photocatalytic activity of gC_3N_4 samples.[12]

Over the past years, SACs have demonstrated outstanding catalytic activities and product selectivity in important transformations, such as alkyne hydrogenation, water oxidation, Suzuki carbon–carbon coupling, water-gas shift, and electrosynthesis.[13] Within the field of pharmaceutical degradation, the use of gC_3N_4-based SACs has been occasionally reported for the photocatalytic degradation of organic pollutants. Wang et al.[14] described a heterogeneous catalyst consisting of highly dispersed Ag atoms and carbon quantum dots on ultrathin gC_3N_4 for the broad-spectrum (UV, visible, and near-infrared light) degradation of naproxen. The authors reached 87% degradation of the pollutant after 25 min of batch irradiation. Unfortunately, the contribution of UV and near-infrared irradiation was not decoupled from that of visible light, and it was thus difficult to understand whether the decomposition occurred due to the UV light. Similarly, Trofimovaite et al.[15] entrapped Pd single atoms on mesoporous TiO_2 to promote the degradation of methyl orange, obtaining 90% removal after 2 h. The photocatalytic data for the nanomaterials was sixfold higher than that of the same catalyst without Cu doping, pointing to the key role of isolated species in the reaction. Unfortunately, such works only explored the contaminant degradation without assessing the extent of (by)product formation during the reaction, leaving gaps in our understanding of the selectivity cycle and demonstrating that, at present, the application of SACs in the photocatalytic degradation of pollutants is in its infancy.[16] An important aspect when using SACs to catalyze the removal of pharmaceuticals concerns the nature of the transition metals entrapped on the porous carrier. Often, rare metals such as Pd, Pt, Ir, Ag, and Au are used in single-atom catalysis,[9] rendering these materials far from meeting some of the most recent green-chemistry guidelines. Trying to fill a knowledge gap, this work demonstrates that by designing an advanced photocatalyst surface and incorporating atomically dispersed and Earth-abundant nickel species on carbon nitride nanosheets, it is possible to control and selectively direct the contaminant degradation, shifting the reaction to the formation of thermodynamically stable gaseous species. This enables a lower extent of noxious benzenic byproduct formation.[17] To decipher the role of atom coordination on the catalytic cycle, we have prepared, characterized, and kinetically compared single-atom and nanoparticle-based Ni catalysts, showing that the effects over single-atom materials are unique and not observed over conventional nanoparticle-based counterparts. This opens directions for the rational design of selective photocatalysts for advanced oxidation processes.

2. Results and Discussion

2.1. Catalyst Characterization

Following the synthetic recipe reported in the Experimental Section, four materials were prepared: carbon nitride in graphitic form (herein indicated as gC_3N_4), carbon nitride in nanosheet form (herein indicated as nC_3N_4), a single-atom Ni-based catalyst on carbon nitride nanosheets (herein indicated as saNi-nC_3N_4), and Ni nanoparticles on carbon nitride nanosheets (herein indicated as nanoNi-nC_3N_4).

The bulk composition, phase purity, and structure of the synthesized samples were analyzed by X-ray powder diffraction (**Figure 1**a). In the prepared materials, two distinct diffraction peaks at 2θ of 12.75° and 27.50° can be indexed, corresponding to the (100) and (002) planes, respectively. These two peaks match well those in the literature,[18] and correspond to graphite-like carbon nitride in the planar-packed system (JCPDS 87-1526). In particular, the sharp diffraction peak at 27.50° is indicative of the typical interplanar stacking of aromatic structures, and the weak peak at 12.75° corresponds to an interplanar structural packing (trigonal N linkage of the tri-s-triazine) motif.

Compared to gC_3N_4, the (002) diffraction peaks for nC_3N_4, saNi-nC_3N_4, and nanoNi-nC_3N_4 are narrower, pointing to an increased degree of material condensation, which is common in highly crystalline nanosheet-based materials. Comparatively,

Prof. A. Sroka-Bartnicka
Institute of Biological Sciences
Maria Curie-Sklodowska University
Akademicka 19, 20-033 Lublin, Poland

Dr. I. S. Pieta
Institute of Physical Chemistry
Polish Academy of Sciences
01-224 Warsaw, Poland

Prof. R. Zbořil
Nanotechnology Centre, CEET
VŠB-Technical University of Ostrava
17. listopadu 2172/15, 708 00 Ostrava-Poruba, Czech Republic

Dr. M. B. Gawande
Department of Industrial and Engineering Chemistry
Institute of Chemical Technology
Mumbai-Marathwada Campus
Jalna 431213, Maharashtra, India
E-mail: mb.gawande@marj.ictmumbai.edu.in
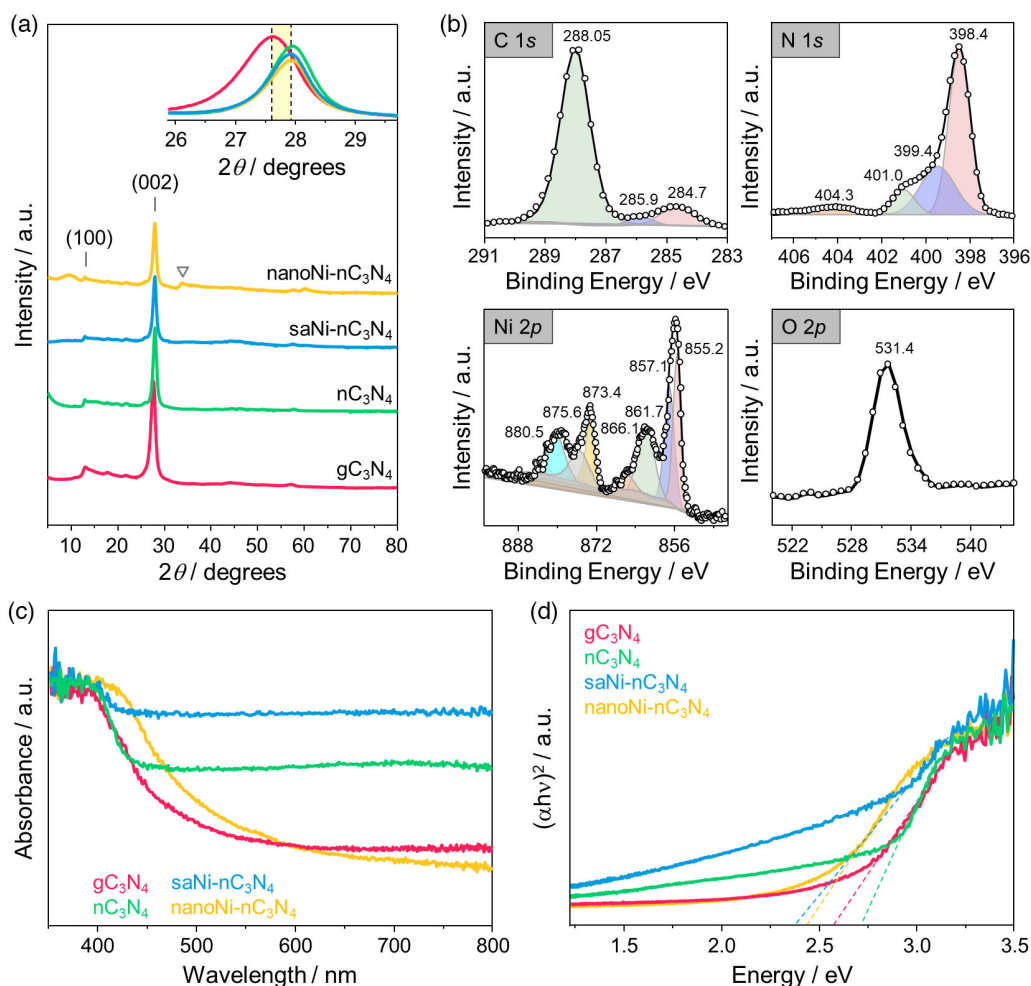
Figure 1. a) Wide-angle XRD patterns of the different catalysts with an inset showing the shift of the (002) peak to higher angles for nanosheet materials. b) High-resolution C 1s, N 1s, Ni 2p, and O 2p XPS spectra of saNi-nC$_3$N$_4$. c) Visible region of the UV–vis absorption spectra and d) Tauc plot of the different catalysts.

the (002) diffraction peak of nC$_3$N$_4$, saNi-nC$_3$N$_4$, and nanoNi-nC$_3$N$_4$ shift slightly toward higher angles compared to gC$_3$N$_4$ (from 27.50° to 27.90°; see the inset in Figure 1a), indicating that the interlayer distance between the basic sheets of gC$_3$N$_4$ is smaller as the crystal structure tends to become more stable due to the increase in calcination temperature with a slower rate during synthesis.[19–21] Apart from peaks that can be indexed to C$_3$N$_4$, no additional peaks for metallic or oxidic Ni species are observed in saNi-nC$_3$N$_4$, indicating that Ni is evenly dispersed.[22,23] On the contrary, nanoNi-nC$_3$N$_4$ has a small reflection at 34° (indicated in Figure 1a with a triangle) which is assigned to oxidic NiO species.

The hybridized orbital contribution of each element was confirmed by running high-resolution XPS of the synthesized materials. In particular, Figure S2, Supporting Information, shows the XPS spectra of gC$_3$N$_4$ and nC$_3$N$_4$, and Figure 1b shows the spectra of saNi-nC$_3$N$_4$. The complete integration of the XPS peaks is listed in Table S1, Supporting Information. Notably, in gC$_3$N$_4$, the C 1s spectrum can be clearly deconvoluted into three major peaks at 284.44, 285.20, and 287.93 eV (Figure S2, Supporting Information). In particular, the peak at

284.44 eV can be ascribed to graphitic carbon (C—[C,H] adventitious carbon, energy calibration sp^2 carbon), which at 285.20 eV corresponds to sp^3 C—C bonds, while the signal at 287.93 eV can be attributed to sp^2 N—C=N bonds in the aromatic skeleton of the synthesized carbon nitride.[20,21] This confirms that the surface structure of gC$_3$N$_4$ is composed of repeating "melem" units. Notably, the binding signals at 286.45 and 288.49 eV can be attributed to C—O and O—C=O bonds, respectively, indicating the existence of oxygen species in the sample, likely coming from the air calcination at 550 °C. In the XPS spectra of nC$_3$N$_4$, all three C=N, C—N, and N—C=N peaks are observed (Figure S2, Supporting Information). The small shifts to higher binding energies (BEs) confirmed the strong interaction during nanosheet condensation, which is in line with the wide-angle XRD analysis in Figure 1a.[20,21] In the case of saNi-nC$_3$N$_4$, the three major peaks are centered at 284.68, 285.83, and 288.06 eV, which correspond again to graphite sp^2 carbon, sp^3-coordinated carbon bonds C—C, and the N=C—N bond with sp^2, respectively (Figure 1b). However, a complete absence of an oxygen-bounded peak (C—O) is evidenced in this sample. The high-resolution N 1s spectra (Figure 1b) of the same material

show three peaks approximately centered at 398.55, 399.87, 400.93, and 404.20 eV, corresponding to sp^2-hybridized N in triazine rings (C=N—C), pyrrolic tertiary-like N [N—(C)$_3$], free amino groups (C)$_2$—N—H, and the charging effect, respectively.[20,24] However, for saNi-nC$_3$N$_4$, a shift of the pyrrolic N shift at 399.87 eV is noted, which is due to the anchoring of the Ni single atoms to the lone pair of the pyrrolic N atom[25] (Figure 1b). This is confirmed by Ni 2p XPS. In fact, for the case of saNi-nC$_3$N$_4$, the Ni 2p species can be deconvoluted into four major peaks with binding energies of Ni at 857.30, 855.73, 873.33, and 874.90 eV, all corresponding to the Ni 2$p_{3/2}$ and Ni 2$p_{1/2}$ of Ni^{2+}. The results are conducive to the formation of Ni—N$_x$ active sites. Particularly, pyrrolic N tends to coordinate with Ni atoms to form Ni—N$_x$ moieties. This appears to be a characteristic fingerprint of Ni SACs, and differs from other earth-abundant SACs, for example, those made of Fe, where pyridinic N species are involved in the coordination of the isolated metals.[26–28] Notably, the shift in Ni 2$p_{3/2}$ and Ni 2$p_{1/2}$ is a low-valent oxidation state due to the anchoring nature of the single atoms, as reported in previous studies.[29–31] This resolves the question on the nature of the active site, pointing to the presence of only cationic Ni^{2+} species. If metallic Ni active sites were present, a Ni 2$p_{3/2}$ contribution at 852.6 eV, corresponding to subsurface Ni^0 species, would be expected, which is absent in our case.[31] X-ray absorption near-edge spectroscopy (XANES) confirmed the XPS results, proving that only cationic Ni^{2+} species are present (Figure S3, Supporting Information). Extended X-ray absorption fine structure (EXAFS) spectroscopy has been applied
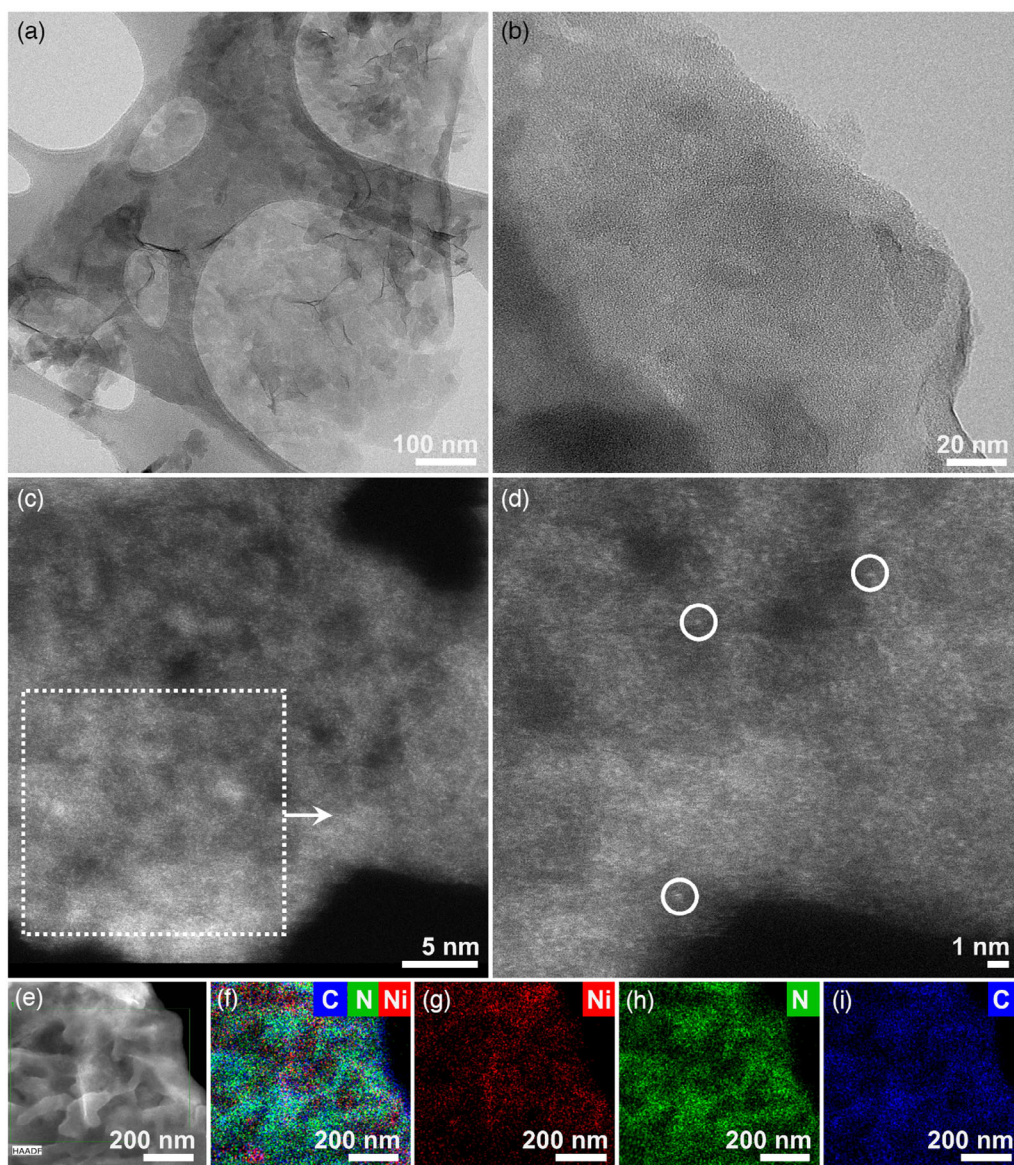
Figure 2. HRTEM micrographs of saNi-nC$_3$N$_4$ at magnifications of a) 100 nm and b) 20 nm, showing the absence of metal nanoparticles. c) High-resolution HAADF-STEM micrographs of the same catalyst and d) higher magnification of a portion of it. e–i) HAADF-STEM elemental mapping showing the individual contribution of C, N, and Ni on a saNi-nC$_3$N$_4$ catalyst area.

to determine the local structure of the Ni-based catalysts (Figure S3, Supporting Information). The pseudoradial distribution function for saNi-nC$_3$N$_4$ shows a main contribution, which was best fitted by Ni—N neighbors at 2.082 Å (Table S2, Supporting Information), in agreement with the XPS, characteristic of Ni atoms in the nC$_3$N$_4$ cavities, and most likely of single-atom character. Another Ni—N contribution can be fitted at 2.444 Å, which indicates Ni to be present in the interstitial or interplanar layers of the nC$_3$N$_4$. The third peak is fitted at 3.103 Å, with three nearest-neighbor Ni atoms, suggesting that apart from single Ni atoms also Ni single-site species in the form of Ni—O—Ni clusters are present, which are most likely formed in the interstitial layers. The XAS characterization of the nanoNi-nC$_3$N$_4$ shows only two peaks: The first is fitted with Ni—O neighbors at 2.056 Å and the second with the Ni—O—Ni clusters above. The close vicinity of the Ni—N and Ni—O is a typical limitation of XAS characterizations over SACs made of earth-abundant elements.[32] Transmission electron microscopy corroborates this result and further demonstrates the absence of any nickel-based nanoparticles on the surface of an SAC (Figure 2a–c). Furthermore, the HAADF-STEM images in Figure 2d–i reveal that individual nickel atoms are atomically dispersed, proving a homogenous distribution of the active phase over the entire nC$_3$N$_4$ nanosheet structure. The Ni single atoms are highlighted with white dotted circles in the high-resolution STEM image (Figure 2j). Comparing this micrograph and those for nanoNi-nC$_3$N$_4$ in Figure S4, Supporting Information, the absence of any Ni clusters or particles in the single-atom material is obvious. The results are consistent with the XRD of saNi-nC$_3$N$_4$, where no clear peaks assignable to bulk species (i.e., nanoparticles or clusters) are observed. Yet EDX elemental analysis (Figures S5 and S6, Supporting Information) confirms the presence of all key elements (including the metal phase) in the samples.

Optical properties of gC$_3$N$_4$, nC$_3$N$_4$, nanoNi-nC$_3$N$_4$, and saNi-nC$_3$N$_4$ have been studied by UV–vis diffuse reflectance spectroscopy, and the results are plotted in Figure 1c. Structural change in gC$_3$N$_4$ can alter light absorption properties, but the spectra resemble literature precedents where UV–vis spectroscopy was applied over similar catalysts.[33] In particular, as shown in Figure 1c, the absorption edge of nC$_3$N$_4$ exhibits a blueshift compared to gC$_3$N$_4$. From the spectra, the sample bandgaps were calculated using the Tauc plot in Figure 1d. In particular, gC$_3$N$_4$, nC$_3$N$_4$, nanoNi-nC$_3$N$_4$, and saNi-nC$_3$N$_4$ show bandgaps of 2.5, 2.6, 2.7, and 2.4 eV, respectively. The observed shift of the absorption edge, going from gC$_3$N$_4$ to nC$_3$N$_4$, might be due to the quantum size effect caused by the ultrathin nanosheet structures of nC$_3$N$_4$.[19,24,34,35] All synthesized materials absorb within the visible region. In particular, introduction of metal single atoms into the nC$_3$N$_4$ has a dual effect of narrowing the optical band gap and enhancing the light absorption in the range 500–800 nm due to the introduction of metal ions, which facilitate ligand-to-metal charge transfer. It is evident that the single-atom Ni catalyst has a narrower bandgap compared to the nanoNi-nC$_3$N$_4$ material, resulting in the enhanced light-harvesting capability of saNi-nC$_3$N$_4$ in the visible light region (i.e., $400 < \lambda < 700$ nm). A narrow bandgap broadens the light response, generating more electrons upon irradiation.[36] As a result, saNi-nC$_3$N$_4$ is expected to show better photocatalytic activity compared to the other samples because of its lower bandgap, the enhanced average life of the photogenerated electron–hole pair, and easy electron transfer between the single-atom Ni and the carbon nitride carrier.

2.2. Catalyst Performance and Physicochemical Correlations

Using the materials described previously, we explored the photocatalytic removal of pharmaceuticals in deionized water at a pollutant concentration of 100 ppm. Gemfibrozil, a major contaminant present in hospital and civil wastewater effluents, was taken as a model compound to assess the degradation of water pollutants of emerging concerns. This small molecule is difficult to photo-oxidize and previous studies have shown that its benzene core cannot be degraded, resulting in the formation of genotoxic moieties in the liquid solution.[1,4]

Our catalytic tests have been conducted under photocatalytic batch conditions. As shown in **Figure 3**a, the removal of gemfibrozil increases with longer irradiation times over all catalysts. After 30 min of visible light irradiation, the removal efficiency is 32.0%, 36.2%, 53.5%, and 75.9% for gC$_3$N$_4$, nC$_3$N$_4$, nanoNi-nC$_3$N$_4$, and saNi-nC$_3$N$_4$, respectively. Therefore, the order of reactivity among the catalysts is saNi-nC$_3$N$_4$ > nanoNi-nC$_3$N$_4$ > nC$_3$N$_4$ and gC$_3$N$_4$. It is interesting to observe that no degradation occurs in the absence of light (Figure 3a), proving that gemfibrozil degradation is driven by photocatalysis. Also, the order of reactivity does not change on fixing the residence time and varying the temperature and pressure (Figure S7, Supporting Information) and is thus independent of the specific experimental conditions; furthermore, the performance is stable upon catalyst recycling (Figure 3b), which attests no loss of the active sites and no structural rearrangements in the Ni—N$_x$ motifs after use. We evaluated the catalyst leaching resistance after the tests in Figure 3b, determining the metal content in the liquid solution after each reaction. In all cases, the amount of leached Ni in the saNi-nC$_3$N$_4$ was lower than the detection limit of ICP-MS (<0.001 mg L^{-1}), which meets the total (toxic) nickel emission standards in Europe (requiring this to be lower than 0.5 mg L^{-1}).[37] Finally, the superiority of the saNi-nC$_3$N$_4$ material can be appreciated in a vis-à-vis comparison with an industrially used TiO$_2$ catalyst. Whereas in the case of TiO$_2$ the degradation efficiency is below 10% after 30 min of visible light irradiation, pure nC$_3$N$_4$ and in particular saNi-nC$_3$N$_4$ stand up for efficiency, reaching 36.2%, and 75.9% degradation, respectively (Figure S8, Supporting Information). Table S3, Supporting Information, generalizes the conclusions for gemfibrozil to other contaminants.

Based on the data in Figure 3a, it is possible to model the degradation of a pharmaceutical compound. In particular, for an ideal isothermal catalytic batch reactor, the general material balance equation is given by Equation (1)

$$\frac{dN_i}{dt} = \frac{d(V_{batch} c_i)}{dt} = V_{batch} \frac{dc_i}{dt} = -r \tag{1}$$

where N_i represents the number of moles of the compound i, V_{batch} is the reactor volume, c_i is the concentration of the compound i, and r represents the reaction rate. However, the reaction rate over a solid catalytic system can be expressed with Equation (2)

$$r = m_{cat} k_{int} c_i \tag{2}$$
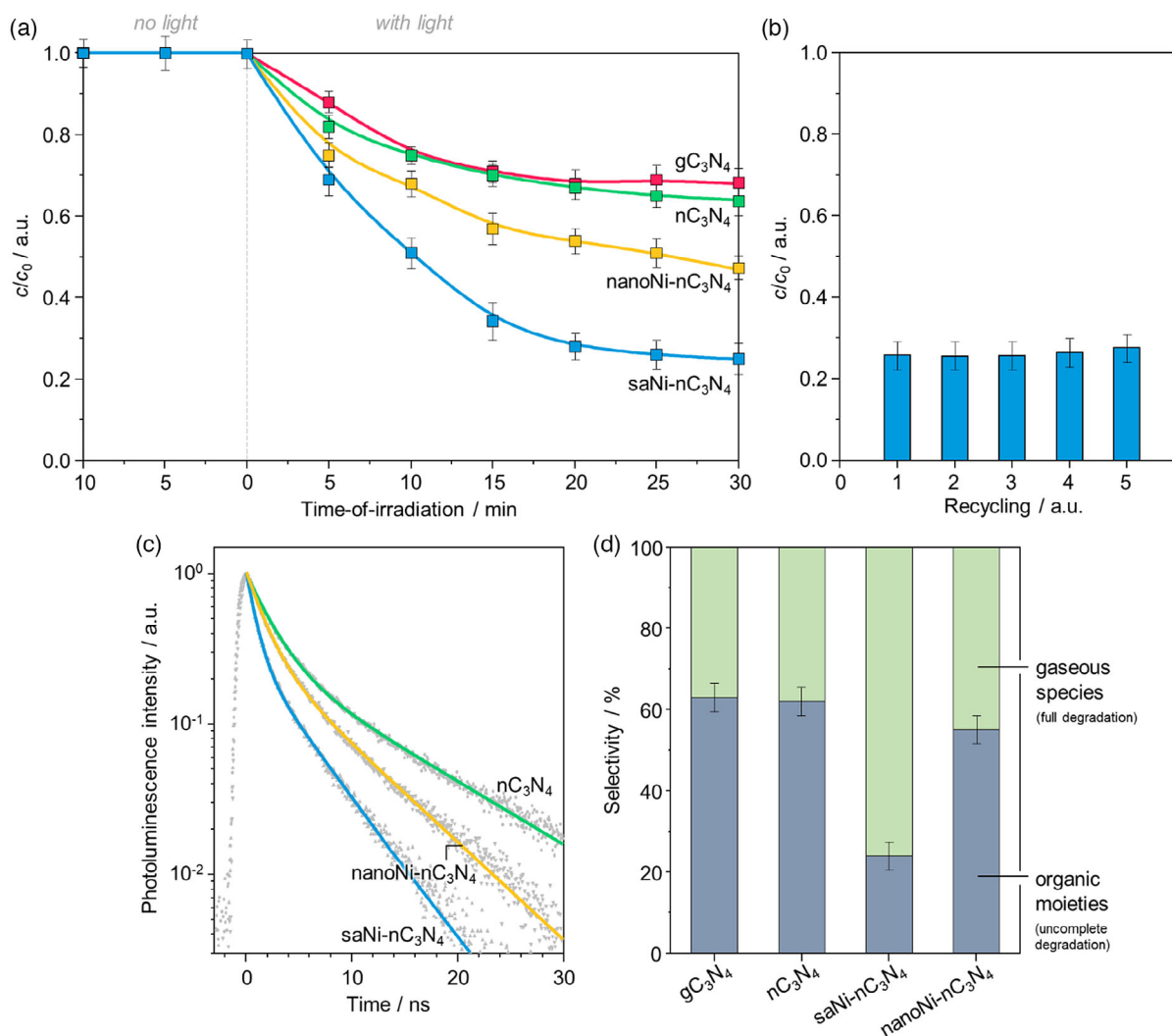
Figure 3. a) Influence of the irradiation time on the degradation of gemfibrozil in water over the different catalysts in the absence and presence of light ($\lambda = 400$ nm), at [gemfibrozil] = 100 ppm, temperature = 30 °C, and pressure = 3 bar. The figure highlights the contribution of light in the catalytic process. b) Stability test over saNi-nC$_3$N$_4$ during five consecutive runs of gemfibrozil degradation at temperature $T = 30$ °C, pressure $P = 3$ bar, and irradiation time = 30 min. c) Time-resolved photoluminescence spectra of nC$_3$N$_4$, nanoNi-nC$_3$N$_4$, and saNi-nC$_3$N$_4$. d) Selectivity to gaseous species and leftover organic moieties over the different catalysts. Additional catalytic tests with alternative conditions and contaminants are included in the Supporting Information.

Table 1. Kinetic (k) and equilibrium (K) constants, as well as half-life time for the degradation of gemfibrozil in water over different catalysts. Experimental conditions are in figure 3a.

Catalyst	Pseudo-first-order concentration decay			Langmuir–Hinshelwood expression	
	k' [s^{-1}]	k [m^3 g$_{cat}^{-1}$ s^{-1}]	$t_{1/2}$ [min]	k_{int} [g g$_{cat}^{-1}$ s^{-1}]	K_{LH} [m^3 g^{-1}]
gC$_3$N$_4$	4.25×10^{-4}	4.25×10^{-7}	27.1	4.03×10^{-2}	1.06×10^{-5}
nC$_3$N$_4$	4.53×10^{-4}	4.53×10^{-7}	24.8	4.23×10^{-2}	1.06×10^{-5}
saNi-nC$_3$N$_4$	11.8×10^{-4}	11.8×10^{-7}	9.6	9.35×10^{-2}	1.26×10^{-5}
nanoNi-nC$_3$N$_4$	6.86×10^{-4}	6.86×10^{-7}	16.6	6.30×10^{-2}	1.08×10^{-5}

where m_{cat} is the catalyst mass and k_{int} represents the intrinsic kinetic constant. Combining Equation (1) and (2), it is possible

to obtain the general material balance equation for a batch reactor (Equation (3))

$$\frac{\mathrm{d}c_i}{\mathrm{d}t} = -\frac{m_{\mathrm{cat}}}{V_{\mathrm{batch}}} k_{\mathrm{int}} c_i \tag{3}$$

Solving this ordinary differential equation, the analytic solution is given by Equation (4)

$$c = c_0 \exp\left(-\frac{m_{\mathrm{cat}}}{V_{\mathrm{batch}}} k_{\mathrm{int}} t\right) = c_0 \exp(-k' t) \tag{4}$$

This equation corresponds to the classical pseudo-first-order concentration decay used to model the behavior of a batch reactor. The k' variable provides valuable information on how fast this reduction is and, therefore, how fast gemfibrozil is being removed from water. Considering that a kinetic analysis of gemfibrozil degradation through ab initio simulations has been never reported so far, this approach is one of the available methods to simulate the reactor behavior. Based on the analysis (**Table 1**), the pseudo-first-order kinetic constant for the degradation of gemfibrozil over saNi-nC$_3$N$_4$ is 11.8×10^{-4}, which is three times higher than that over pure gC$_3$N$_4$ and nC$_3$N$_4$ and two times higher than over nanoNi-nC$_3$N$_4$. The estimated half-life time for the contaminant degradation is in line with this result, and further demonstrates that saNi-nC$_3$N$_4$ requires only 9.8 min to halve the contaminant concentration.

We have compared these values with those determined through a Langmuir–Hinshelwood expression, which is a widely used model for describing heterogeneous photocatalytic reactions.[2,3] For a monomolecular irreversible degradation reaction, the intrinsic reaction rate is given by Equation (5)

$$r_{\mathrm{int}} = \frac{k_{\mathrm{int}} m_{\mathrm{cat}} K_{\mathrm{LH}} c}{1 + K_{\mathrm{LH}} c} \tag{5}$$

where k_{int} is the intrinsic rate constant, m_{cat} is the catalyst mass, K_{LH} is the adsorption equilibrium constant of the reactant, and c is the mass concentration of the pollutant in the liquid phase. Therefore, the observed differential change of the bulk concentration c_i during the reaction time t assumes the form in Equation (6)

$$\frac{\mathrm{d}c_i}{\mathrm{d}t} = -\frac{m_{\mathrm{cat}}}{V_{\mathrm{batch}}} k_{\mathrm{int}} \frac{K_{\mathrm{LH}} c_i}{1 + K_{\mathrm{LH}} c_i} \tag{6}$$

The estimate for the constant k_{int} and K_{LH} were obtained from regression fitting the linear region of Figure 3a. The estimated parameters are summarized in Table 1. The model confirms the higher kinetic constants observed over the saNi-nC$_3$N$_4$ catalyst, but similar thermodynamic constants that indicate similar degradation paths over the catalysts. The results from this analysis are particularly relevant, considering that no other catalyst reported to date can degrade gemfibrozil with the same efficiency (Table S4, Supporting Information).

This photocatalytic result can be correlated with the ligand–metal charge transfers in the nanomaterials, as confirmed by the measured photoluminescence (PL) data (Figure 3c). In fact, at a lower PL intensity, the separation rate of the photogenerated electron–hole pairs is higher. A broad PL band between 430 and 480 nm (with the value increasing passing from nC$_3$N$_4$ to saNi-nC$_3$N$_4$) is observed, with long tails approaching 700 nm and sharply decreasing afterward.[38] The PL emission intensity of saNi-nC$_3$N$_4$ and nanoNi-nC$_3$N$_4$ is significantly reduced as compared to pure nC$_3$N$_4$ and gC$_3$N$_4$, indicating that the introduction of a Ni single atom or nanoparticles promotes electron transfer and reduces the photogenerated electron–hole recombination rate via inhibition of charge carrier recombination.[35] However, saNi-nC$_3$N$_4$ holds enhanced PL intensity compared to nanoNi-nC$_3$N$_4$, probably due to the even distribution of Ni in the form of single atoms on the nanosheets of nC$_3$N$_4$. In other words, the high dispersion of Ni in the form of single atoms enhances the separation of the photogenerated e$^-$–h$^+$ pairs, resulting in efficient transport of those during catalysis.[39,40] Time-resolved photoluminescence (TRPL) spectroscopy reveals that the estimated ligand–metal charge transfer lifetimes diminish gradually as Ni single atoms are embedded in the form of nanoparticles over nanosheet nC$_3$N$_4$. The calculated average fluorescence decay lifetimes (τ_{ave}) of nC$_3$N$_4$, nanoNi-nC$_3$N$_4$, and saNi-nC$_3$N$_4$ are 7.4, 4.9, and 3.3 ns, respectively (Figure 3c). Such lifetime behavior is attributed to the emergence of a nonradiative pathway from the possibly formed N—Ni—N interaction in the saNi anchored to the nC$_3$N$_4$ system (see also Figure S9, Supporting Information), which is supported by XPS and EXAFS data analysis and is not observed over nanoNi-nC$_3$N$_4$.

To unravel the extent of product selectivity over the different photocatalysts, we determined the organic content in the solutions using CHN analysis (Figure 3d). It is known in the literature that during photocatalytic degradation of organic contaminants, benzenic organic moieties are formed, and these may be even more toxic than the initial substrate.[4] Our carbon balance analysis shows that gC$_3$N$_4$, nC$_3$N$_4$, and nanoNi-nC$_3$N$_4$ result in a similar content of organic byproducts and in a lower fraction of gaseous species coming from the complete degradation of the pharmaceutical contaminant; in contrast, saNi-nC$_3$N$_4$ results in a higher extent of gaseous products. The results point to a more selective degradation path over "single-atom" Ni species compared to "multiatom" Ni nanoparticles and highlight the need for a rational design of the catalytic surface interface.

Characterization of the used catalysts reveals no significant structural alterations in the samples and confirms a lower deposition of organic moiety over the SAC. No changes in the characteristic XRD peaks are detected in the postreaction samples, supporting the fact that all the synthesized materials, including saNi-nC$_3$N$_4$, are catalytically stable (Figure S10, Supporting Information). The Ni—N sites thus work as a flexible bridge to facilitate the faster electron transfer and enhance the charge density on the Ni single atom, particularly given that no surface alterations are visible by microscopy (Figure S11, Supporting Information).[41] In the used saNi-nC$_3$N$_4$, XPS analysis exhibits the single-atom character is well maintained after reuse of the synthesized material. Herein, the XPS spectrum shows peaks of Ni $2p_{3/2}$ at 855.70 indicating the retention of Ni^{2+} with complete absence of Ni^0 (see Figure S12, Supporting Information). Moreover, in case of N $1s$, binding energy of saNi-nC$_3$N$_4$ XPS analyses exhibited that the pyrrolic N species at 399.58 eV is well maintained, confirming the Ni—N bond existence.[25] Figure S13, Supporting Information, compares the surface state of saNi-nC$_3$N$_4$ before and after the reaction via AFM. The micrographs evidence the presence of a small fraction of organic moieties on the single-atom sample. The catalyst, in particular, has a rough film on it of average roughness $R_{\mathrm{a}} = 124$ nm (Figure S13a,

Supporting Information). The high-magnification micrograph displays a detailed topography of the sample, showing that the catalyst is composed of triangular-like surfaces decorated with globular objects. The saNi-nC$_3$N$_4$ catalyst is supported on carbon nitride, whose original topography, shown in Figure S13b, Supporting Information, is composed of flat flakes with sharp edges. These flakes adhere to each other, forming a multilayer material, which is characteristic of carbon nitride materials. It was evident that the morphology of the saNi-nC$_3$N$_4$ catalyst slightly changes after reaction (Figure S13c, Supporting Information), presumably because of the presence of benzenic deposit material formed during the catalytic cycle. Such deposits, however, are in larger quantities over nanoNi-nC$_3$N$_4$, nC$_3$N$_4$, and gC$_3$N$_4$ as these samples are even less selective and give a higher fraction of organic species (Figure 3). This is confirmed by AFM analysis of nanoNi-nC$_3$N$_4$ (Figure S14, Supporting Information). Here, the average roughness is higher than in the case of saNi-nC$_3$N$_4$. The stacked flat flakes observed in the pristine support, characteristic of graphite materials, leave space for globular objects, which are now much more visible and are 20–30 nm higher in height than in the case of saNi-nC$_3$N$_4$. The AFM results prove in an unprecedented manner the surface deposits during photocatalytic degradation of gemfibrozil; the results also verify the high selectivity expected over SACs and the lower formation of benzenic byproducts over these samples, in line with the catalytic data.

Raman spectroscopy confirms the absence of major structural changes in the samples and provides further insights into the extent of byproducts. In particular, the full spectra of saNi-nC$_3$N$_4$ before and after reaction are shown on **Figure 4**a, and their deconvoluted spectra before and after reaction (both in the 1770–1090 cm^{-1} range) are shown in Figure 4b,c, respectively. Raman band analysis is presented instead in the Supporting Information (Table S5 and S5, Supporting Information). In both pristine and used SACs, bands corresponding to ν(C—C) at $\approx$1145 cm^{-1} and ν(C=C) at $\approx$1472 cm^{-1} are detected.,[42,43] Moreover, two bands at $\approx$1340 and $\approx$1618 cm^{-1}, corresponding to disordered graphite (indicated, respectively, with D and D$'$), and a band at $\approx$1552 cm^{-1}, corresponding to graphite of perfect crystalline structure (indicated with G), are present.[43,44] Because the Ni-based materials are characterized by a 2D structure with various degrees of condensed graphitic domains, the higher fraction of C=C and C—C species can be due to reaction residues.[43,45] The chemical maps of the samples before and after reaction (Figure 4d and S15, Supporting Information) show similar distributions of the C—C, D, C=C, G, and D$'$ bands across the investigated region. However, the ratio of the band area of ν(C—C) to ν(C=C), calculated and reported in Table S5 and S6, Supporting Information, shows an increase of C—C bonds over both nanoNi-nC$_3$N$_4$ and saNi-nC$_3$N$_4$. Based on the reported degradation path of gemfibrozil (Figure S16, Supporting Information), we can speculate that
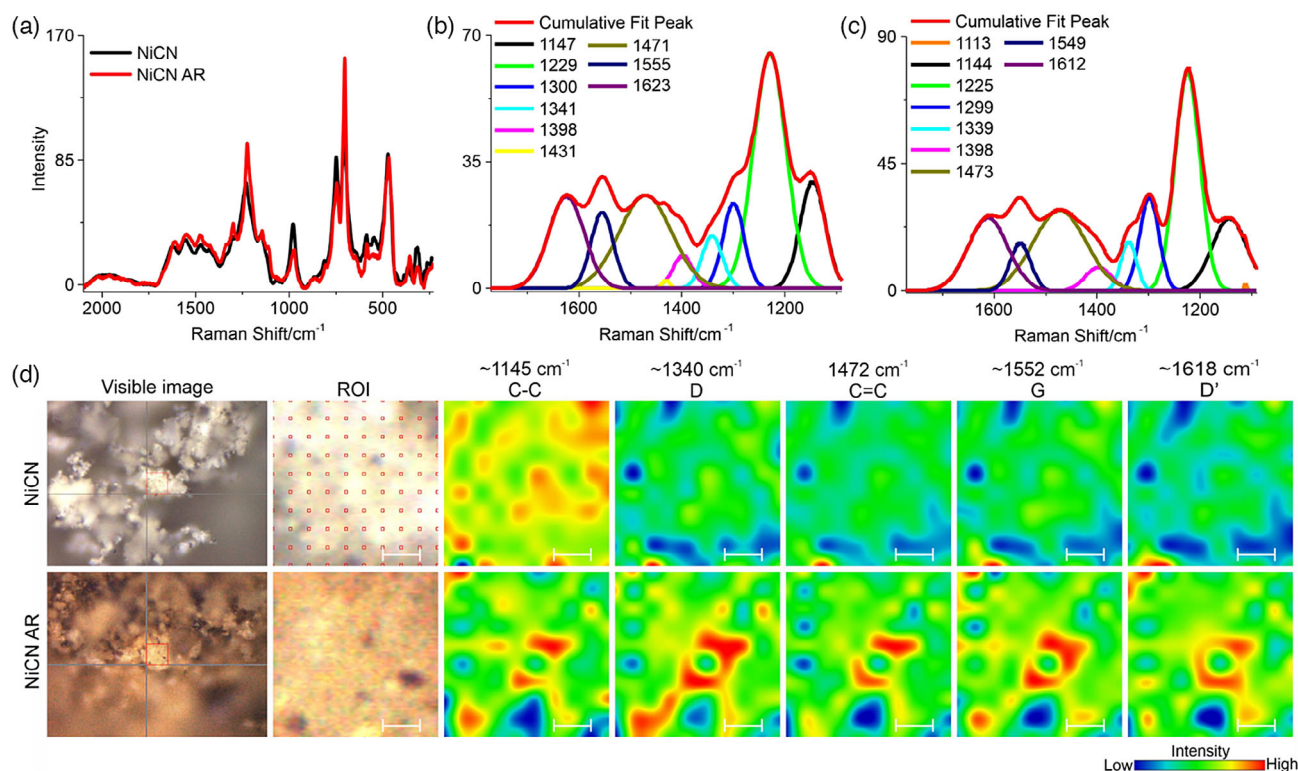
Figure 4. a) Raman spectra of saNi-nC$_3$N$_4$ before (black) and after (red) reaction. Enlargement of the 1700–1090 cm^{-1} region b) before and c) after reaction, with the cumulative spectrum in red and the deconvoluted bands in other colors. d) Raman maps with the marked region of interest (ROI), showing the distribution of selected bands of saNi-nC$_3$N$_4$ before (first line) and after (second line) reaction. The white scale bar in (d) corresponds to 3 µm. The symbols D and D$'$ indicate the bands of disordered graphite, and G refers to graphite of perfect crystalline structure.

these residues are small compounds coming from late-stage decomposition steps. The complete identification of the type of contaminants formed is beyond the scope of this contribution, which focuses on a novel catalytic system with unprecedented surface properties and catalytic performance, and will be the focus of follow-up advanced studies.

3. Conclusion

We have studied the preparation, characterization, and photocatalytic performance of an earth-abundant heterogeneous catalyst featuring nanoparticle-based and highly dispersed Ni over nanosheets of graphitic carbon nitride. The highly dispersed character of the sample has been confirmed by spectrometric measurements, showing synergism interfacial carrier–metal transfer due to the Ni—N environment. By combining advanced characterization tools with kinetic investigations, we have demonstrated that these newly formed isolated single atoms of Ni facilitate the electron transfer, increasing the charge density on Ni, and reducing the photocarrier transfer barrier. This improves the degradation of gemfibrozil, a model pharmaceutical pollutant found in wastewater, reducing the formation of toxic benzenic byproducts during photooxidation. This effect, which is not observed over conventional nanoparticle-based catalysts, was confirmed by characterization of the used catalyst via Raman and AFM. This research work opens new avenues in designing selective photocatalysts for advanced oxidation processes, showing the importance of charge transfer to control the surface catalytic properties of novel engineered nanomaterials.

4. Experimental Section

Synthesis: Dicyandiamide, Millipore water ($18\,M\Omega\,cm^{-1}$), and $Ni(NO_3)_2\cdot6H_2O$ were purchased from Sigma-Aldrich and used as such, without any further purification. The synthesis of gC_3N_4 was performed using dicyanamide as a source of carbon and nitrogen. In a typical experiment, 10 g of dicyanamide was placed in an alumina crucible and heated in air at $550\,°C$ for 3 h (heating rate of $10\,°C\,min^{-1}$).[24] The nC_3N_4 nanosheets were prepared as reported elsewhere, and a schematic representation of the process is shown in Figure S1, Supporting Information.[18] Briefly, 1 g of gC_3N_4 was spread in the alumina crucible with good contact between gC_3N_4 and air, and then heated at $520\,°C$ for 4.5 h using a heating rate of $2\,°C\,min^{-1}$. A pale-yellow powdered material was obtained. The nanosheets of carbon nitride were used as such as photoactive support for the dispersion of nickel species. In particular, $Ni(NO_3)_2\cdot6H_2O$ in (Millipore) water (200 mg, 20 mL) was added dropwise to nC_3N_4 (500 mg), and the suspension was kept under sonication for 30 min. At the end of this step, the suspension was left for 12 h at ambient temperature. Then, 1.5 g of sodium borohydride ($NaBH_4$) was added, and the reaction mixture was stirred for another 12 h at $80\,°C$, followed by ten runs (each of 2 min) of rapid microwave heating (LG, power 1000 W; P/No MEZ66853207). The authenticity of the obtained SAC (herein indicated as "saNi-nC_3N_4") was confirmed through in-depth characterization (vide infra). Nickel nanoparticles over nC_3N_4 were formulated by conventional incipient wetness impregnation of nC_3N_4 with an aqueous solution (10 mL) of nickel nitrate $Ni(NO_3)_2\cdot6H_2O$ (200 mg), followed by drying at $65\,°C$ for 2 h and calcination at $200\,°C$ for 3 h. The latter catalyst is indicated as "nanoNi-nC_3N_4." Over both materials, the loading of Ni was confirmed by inductively coupled plasma mass spectrometry (ICP-MS) and resulted to be 8 wt% for both saNi-nC_3N_4 and nanoNi-nC_3N_4.

Characterization: Powder X-ray diffraction (XRD) patterns were collected over an X'Pert PRO MPD diffractometer (PANalytical) in the Bragg–Brentano geometry, equipped with an X'Celerator detector programmable divergence, and diffracted beam antiscatter slits at room temperature. For the XRD patterns, iron-filtered Co Kα radiation (40 kV, 30 mA, $\lambda = 0.1789\,nm$) was used. The angular range of measurement was set as $2\theta = 5°–90°$, with a step size of $0.017°$. The Ni content in the fresh and used catalysts was determined by ICP-MS on an Agilent 7700x (Agilent, Japan). A weighted amount of sample from the catalyst (0.01 mg, Kern ABT 220-5DNM) was digested with nitric acid in a microwave digester. High-resolution transmission electron microscopy (HRTEM) images were obtained over a Titan G2 60-300 microscope (FEI), equipped with an X-FEG-type emission gun operating at 300 kV. High-angle annular dark-field detector (HAADF) scanning transmission electron microscopy (STEM) analysis was conducted over a Titan G2 60-300 microscope (FEI), equipped with HAADF detector 3000 (Fishione). Elemental mappings were obtained via energy-dispersive spectrometry (EDS) performed in STEM mode on the Super-X system, using four silicon drift detectors (Bruker) and an acquisition time of 20 min. For all microscopy analyses, the samples were dispersed in a mixture of water: ethanol (50:50) and sonicated for 10 min. One drop was then placed on a Cu grid with a holey carbon film and dried in air at room temperature. Surface investigations based on high-resolution X-ray photoelectron spectroscopy (XPS) were performed on the PHI 5000 Versa Probe II XPS system (Physical Electronics) with a monochromatic Al Kα source (15 kV, 50 W) and photon energy of 1486.7 eV. Dual-beam charge compensation was used for all measurements. All spectra were measured in a vacuum ($1.3 \times 10^{-7}\,Pa$) and at a temperature of $21\,°C$. The analyzed area on each sample was a spot of 200 μm diameter. The survey spectra were measured with a pass energy of 187.850 eV and electronvolt step of 0.8 eV, and for the high-resolution spectra, a pass energy of 23.500 eV and an electronvolt step of 0.2 eV were used. The spectra were evaluated with the MultiPak (Ulvac – PHI Inc.) software. All binding energy (BE) values were referenced to the carbon peak C 1s at 284.80 eV. X-ray absorption spectroscopy (XAS) at the Ni K edge was recorded at the SuperXAS beamline of the Swiss Light Source (Paul Scherrer Institut, Villigen, Switzerland). Measurements were performed ex situ in transmission mode on pellets, and a Ni foil was measured simultaneously for absolute energy calibration. The quick-EXAFS (QEXAFS) method was used to collect 100 spectra in 100 s, which were then merged. Athena of the Demeter software package was used for normalization and background subtraction. The fit of the EXAFS spectra was performed by using the NiO structure for the path description. The amplitude reduction factor was calculated from EXAFS fits of the Ni reference foil assuming a coordination number of 12 and amounted to $S_{0,Ni}^2 = 0.95$. The metal content of the fresh and reused catalyst was determined through atomic absorption spectroscopy (AAS). For the analysis, a weighted amount of sample from the catalyst (on a 0.01 mg read-out balance, Kern ABT 220-5DNM) was digested with nitric acid in a microwave digester followed by dilution with water. Photoluminescence (PL) measurements were performed on an FLS980 fluorescence spectrometer (Edinburgh Instruments) equipped with an R928P photomultiplier in a thermoelectrically cooled housing (Hamamatsu Photonics), with a 450 W xenon-arc lamp as the excitation source for steady-state spectra and an EPL-375 ps pulsed diode laser ($\lambda_{em} = 372\,nm$ with a pulse width of 66.5 ps, a repetition rate of 20 MHz, and an average power of 75 μW; Edinburgh Instruments) in conjunction with a time-correlated single-photon counting system for time-resolved measurements. The obtained PL decay curves were fitted using a three-exponential function (Equation (7))

$$I(t) = \sum_{i=1}^{3} B_i \exp\left(-\frac{t}{\tau_i}\right), \text{ with } \sum_{i=1}^{3} B_i = 1 \tag{7}$$

In this expression, τ_i represents the decay time constants, and B_i represents the normalized amplitudes of each component. The amplitude-weighted average decay lifetime, τ_{avg}, for the entire fluorescence decay process was calculated using Equation (8)

$$\tau_{avg} = \frac{\tau_i B_i}{\sum \tau_i B_i} \tag{8}$$

Atomic force microscopy (AFM) was performed by suspending the catalyst in ethanol (50 mL with a catalyst concentration of 5 mg mL^{-1}) and drop casting the suspension on a freshly cleaved highly oriented pyrolytic graphite (HOPG) surface. The sample was dried in an oven at 50 °C for 2 h until the solvent was evaporated. The dry sample was imaged under ambient conditions with AFM in the PeakForce quantitative nanomechanical mapping (PF-QNM) mode using a MultiMode 8 system (Bruker) equipped with an E scanner. RTESPA probes (Bruker) of the nominal resonant frequency of 300 kHz, a nominal spring constant of 40 N m^{-1}, and a nominal tip-end radius of 8 nm were used. All AFM images were processed and analyzed using NanoScope Analysis of Bruker software. The Raman data were collected using a confocal Thermo DXR Raman Microscope with a 50× air objective, and all parameters were optimized to obtain the best signal-to-noise ratio. The laser had a 532 nm wavelength, its power was 8 mW, and the aperture was set to a 50 µm pinhole, with an exposure time of 4 s. The number of exposures for one spectrum was 15. All the samples were measured in the range 100–3400 cm^{-1}. The chemical maps were made with a step size 1.5 µm in x and y directions, resulting in a whole map region of 15 µm × 15 µm. The depth line maps were made with a step size of 2 µm on the x- and z-axis. The whole map area was 10 µm × 20 µm. The analysis of the spectra (i.e., baseline correction and deconvolution) was performed using the Origin Pro software (v. 9.1, OriginLab Corporation, USA) and the Omnic software (v. 8.2, Thermo Fischer Scientific Inc., USA). All maps were normalized prior to the analysis.

Testing and Kinetic Modeling: The photocatalytic performance of the prepared materials was studied evaluating the degradation of a model contaminant in deionized water. Gemfibrozil (10 mg, Sigma-Aldrich, powder, purity level 100%) was dissolved in deionized water (100 mL), and the product was sonicated for 10 min for complete solubilization. This concentration was chosen as it represents the typical level detected in domestic and hospital wastewater effluents, at which gemfibrozil starts to show toxicity in animals.[46] All experiments were conducted using LED lamps, working in the visible light region at 400 nm. The aqueous mixture containing the pharmaceutical contaminant and the catalyst (100 mg) was placed into a round-bottom flask and irradiated using LED lamps placed along each side of the flask. A stream of air was placed close to the reactor to avoid undesired heat generation due to the presence of the LED. The product solutions were analyzed by a high-performance liquid chromatograph (Waters 1525 Binary HPLC pump). The stationary phase consisted of a Purospher Star RP-18 column (250 mm × 4.6 mm, 5 µm). The eluent phase was a mixture of water and methanol with a gradient concentration at a flow rate of 1.0 mL min^{-1}. HPLC calibration curves using a commercial gemfibrozil analytical standard (Sigma-Aldrich, 100 mg standard, 100%) were derived for quantification purposes. The concentration, conversion, and selectivity were calculated by the peak area method. Product solutions were also measured by elemental carbon, hydrogen, and nitrogen (CHN) analysis (2400 CHN, Perkin Elmer) to assess the amount of leftover byproducts coming from incomplete or unselective drug degradation.

The estimates for the kinetic and thermodynamic constants were obtained from the pseudo-first-order concentration decay and also via the Langmuir–Hinshelwood kinetic model. The optimization was conducted using the lsqnonlin optimization algorithm in Matlab, which minimizes the weighted least squares (RSS), based on the expression $\text{RSS} = \sum_i \left[\left(c_{b,i}^{\exp} - C_{b,i}^{\text{model}} \right) / \Delta c_{b,i}^{\exp} \right]^2$ between experimental and calculated concentration data, $c_{b,i}$. The differential equation was solved using the ODE23s solver. After estimation of the optimal parameters, a sensitivity validation was applied by means of perturbation analysis, based on the sum-of-square-errors (SSE) formula, $\text{SSE} = \sum_i (c_{b,i}^{\exp} - c_{b,i}^{\text{model}})^2$, which evaluates the percentage of perturbation against the corresponding value of the objective function.

Supporting Information

Supporting Information is available from the Wiley Online Library or from the author.

Conflict of Interest

The authors declare no conflict of interest.

Author Contributions

G.V. conceived the work. G.V. and M.B.G. coordinated all stages of this research. P.S. prepared samples. P.S., M.N., A.S.-B., O.T., M.P., J.F., I.S.P., and G.V. conducted structural and catalytic characterizations. F.T., D.M., and G.V. performed microkinetic modeling. P.S., I.S.P, R.Z., M.B.G., and G.V. interpreted the data and wrote the manuscript. All authors have given approval to the final version of the manuscript.

Data Availabiity Statement

The data that support the findings of this study are available from the corresponding authors upon reasonable request.

[1] a) UN-Water & The World Health Organization, The United Nations World Water Development Report, **2019**. b) G. Vilé, *Catal. Sci. Technol.* **2020**, *11*, 43.

[2] a) T. Hwa Jeon, M. Seok Koo, H. Kim, W. Choi, *ACS Catal.* **2018**, *8*, 11542. b) S. Cao, M. Du, Y. Li, X. Ye, Y. Wang, J. Ye, *ACS Appl. Nano Mater.* **2020**, *3*, 4197; c) F. Deng, L. Zhao, X. Luo, S. Luo, D. Dionysiou, *Chem. Eng. J.* **2020**, *333*, 423; d) A. Nagar, T. Pradeep, *ACS Nano* **2020**, *14*, 6420.

[3] a) G. Odling, N. Robertson, *ChemSusChem* **2015**, *8*, 1838; b) C. Courtois, C. A. Walenta, M. Tschurl, U. Heiz, C. M. Friend, *J. Am. Chem. Soc.* **2020**, *142*, 13072; c) D. Wang, T. Sheng, J. Chen, H.-F. Wang, P. Hu, *Nat. Catal.* **2018**, *1*, 291.

[4] P. Chen, F. Wang, Z.-F. Chen, Q. Zhang, Y. Su, L. Shen, K. Yao, Y. Liu, Z. Cai, W. Lv, G. Liu, _Appl. Catal. B_ **2017**, _204_, 250.

[5] a) C. Gao, J. Low, R. Long, T. Kong, J. Zhu, Y. Xiong, _Chem. Rev._ **2020**, _120_, 12175; b) P. Li, G. Xiao, Y. Zhao, H. Su, _ACS Catal._ **2020**, _10_, 3640; c) D. Franchi, Z. Amara, _ACS Sustain. Chem. Eng._ **2020**, _8_, 15405; d) C. Krishnaraj, H. S. Jena, L. Bourda, A. Laemont, P. Pachfule, J. Roeser, C. V. Chandran, S. Borgmans, S. M. J. Rogge, K. Leus, C. V. Stevens, J. A. Martens, V. Van Speybroeck, E. Breynaert, A. Thomas, P. Van Der Voort, _J. Am. Chem. Soc._ **2020**, _142_, 20107; e) A. Kumar, A. Kumar, V. Krishnan, _ACS Catal._ **2020**, _10_, 10253; f) Y. Lin, C. P. Yang, S. H. Wu, X. Li, Y. J. Chen, W. L. Yang, _Adv. Funct. Mater._ **2020**, _30_, 2002918; g) Y. Lin, H. Liu, C. Yang, X. Wu, C. Du, L. Jiang, Y. Zhong, _Appl. Catal. B_ **2020**, _264_, 118479.

[6] a) J. Ran, W. Guo, H. Wang, B. Zhu, J. Yu, S. Qiao, _Adv. Mater._ **2018**, _30_, 1800128; b) J. Li, D. Wu, J. Iocozzia, H. Du, X. Liu, Y. Yuan, W. Zhou, Z. Li, Z. Xue, Z. Lin, _Angew. Chem. Int. Ed._ **2019**, _58_, 1985.

[7] a) A. Wang, J. Li, T. Zhang, _Nat. Rev. Chem._ **2018**, _2_, 65; b) X. Zhang, Z. Sun, B. Wang, Y. Tang, L. Nguyen, Y. Li, F. F. Tao, _J. Am. Chem. Soc._ **2018**, _140_, 954; c) K.-i. Otake, Y. Cui, C. T. Buru, Z. Li, J. T. Hupp, O. K. Farha, _J. Am. Chem. Soc._ **2018**, _140_, 8652; d) Z. Zhang, Y. Chen, L. Zhou, C. Chen, Z. Han, B. Zhang, Q. Wu, L. Yang, L. Du, Y. Bu, P. Wang, X. Wang, H. Yang, Z. Hu, _Nat. Commun._ **2019**, _10_, 1657; e) A. Bakandritsos, R. G. Kadam, P. Kumar, G. Zoppellaro, M. Medved, J. Tuček, T. Montini, O. Tomanec, P. Andrýsková, B. Drahoš, R. S. Varma, M. Otyepka, M. B. Gawande, P. Fornasiero, R. Zbořil, _Adv. Mater._ **2019**, _31_, 1900323; f) S. K. Kaiser, Z. Chen, D. Faust Akl, S. Mitchell, J. Perez-Ramirez, _Chem. Rev._ **2020**, _120_, 11703; g) M. B. Gawande, P. Fornasiero, R. Zbořil, _ACS Catal._ **2020**, _10_, 2231; h) H. Jeong, S. Shin, H. Lee, _ACS Nano_ **2020**, _14_, 14355.

[8] L. Liu, A. Corma, _Chem. Rev._ **2018**, _118_, 4981.

[9] C.-M. Wang, Y.-D. Wang, J.-W. Ge, Z.-K. Xie, _Chem_ **2019**, _5_, 2736.

[10] a) G. Gao, Y. Jiao, E. R. Waclawik, A. Du, _J. Am. Chem. Soc._ **2016**, _138_, 6292; b) S. Wang, J. Li, Q. Li, X. Bai, J. Wang, _Nanoscale_ **2020**, _12_, 364; c) H. Luo, Y. Liu, S. D. Dimitrov, L. Steier, S. Guo, X. Li, J. Feng, F. Xie, Y. Fang, A. Sapelkin, X. Wang, M.-M. Titirici, _J. Mater. Chem. A_ **2020**, _8_, 14690.

[11] a) I. Ghosh, J. Khamrai, A. Savateev, N. Shlapakov, M. Antonietti, B. Konig, _Science_ **2019**, _365_, 360; b) B. Pieber, J. A. Malik, C. Cavedon, S. Gisbertz, A. Savateev, D. Cruz, T. Heil, G. Zhang, P. H. Seeberger, _Angew. Chem. Int. Ed._ **2019**, _58_, 9575-; c) J. Khamrai, I. Ghosh, A. Savateev, M. Antonietti, B. König, _ACS Catal._ **2020**, _10_, 3526; d) C. Cavedon, A. Madani, P. H. Seeberger, B. Pieber, _Org. Lett._ **2019**, _21_, 5331.

[12] W.-J. Ong, L.-L. Tan, Y. H. Ng, S.-T. Yong, S.-P. Chai, _Chem. Rev._ **2016**, _116_, 7159.

[13] a) G. Vilé, D. Albani, M. Nachtegaal, Z. Chen, D. Dontsova, M. Antonietti, N. Lopez, J. Perez-Ramirez, _Angew. Chem. Int. Ed._ **2015**, _54_, 11265; b) A. J. Therrien, A. J. R. Hensley, M. D. Marcinkowski, R. Zhang, F. R. Lucci, B. Coughlin, A. C. Schilling, J.-S. McEwen, E. C. H. Sykes, _Nat. Catal._ **2018**, _1_, 192; c) Z. Chen, E. Vorobyeva, S. Mitchell, E. Fako, M. A. Ortuno, N. Lopez, S. M. Collins, P. A. Midgley, S. Richard, G. Vilé, J. Perez-Ramirez, _Nat. Nanotechnol._ **2018**, _13_, 702; d) W. Ju, A. Bagger, X. Wang, Y. Tsai, F. Luo, T. Möller, H. Wang, J. Rossmeisl, A. S. Varela, P. Strasser, _ACS Energy Lett._ **2019**, _4_, 1663; e) I. S. Pieta, R. G. Kadam, P. Pieta, D. Mrdenovic, R. Nowakowski, A. Bakandritsos, O. Tomanec, M. Petr, M. Otyepka, R. Kostecki, M. A. M. Khan, R. Zboril, M. B. Gawande, _Adv. Mater. Interfaces_ **2021**, _8_, 2001822.

[14] F. Wang, Y. Wang, Y. Feng, Y. Zeng, Z. Xie, Q. Zhang, Y. Su, P. Chen, Y. Liu, K. Yao, W. Lv, G. Liu, _Appl. Catal. B_ **2018**, _221_, 510.

[15] R. Trofimovaite, C.M.A. Parlett, S. Kumar, L. Frattini, M.A. Isaacs, K. Wilson, L. Olivi, B. Coulson, J. Debgupta, R.E. Douthwaite, A.F. Lee, _Appl. Catal. B_ **2018**, _232_, 501.

[16] B. Huang, Z. Wu, H. Zhou, J. Li, C. Zhou, Z. Xiong, Z. Pan, G. Yao, B. Lai, _J. Hazard. Mater._ **2021**, _412_, 125253.

[17] Y. Sun, L. Silvioli, N. R. Sahraie, W. Ju, J. Li, A. Zitolo, S. Li, A. Bagger, L. Arnarson, X. Wang, T. Moeller, D. Bernsmeier, J. Rossmeisl, F. Jaouen, P. Strasser, _J. Am. Chem. Soc._ **2019**, _141_, 12372.

[18] Q. Lin, L. Li, S. Liang, M. Liu, J. Bi, L. Wu, _Appl. Catal. B._ **2015**, _163_, 135.

[19] W. Xing, W. Tu, Z. Han, Y. Hu, Q. Meng, G. Chen, _ACS Energy Lett._ **2018**, _3_, 514.

[20] P. Qiu, H. Chen, C. Xu, N. Zhou, F. Jiang, X. Wang, Y. Fu, _J. Mater. Chem. A_ **2015**, _3_, 24237.

[21] J. Safaei, N. A. Mohamed, M. F. M. Noh, M. F. Soh, M. A. Riza, N. S. M. Mustakim, N. A. Ludin, M. A. Ibrahim, W. N. R. W. Isahak, M. A. M. Teridi, _J. Alloys Compd._ **2018**, _769_, 130.

[22] J. Liu, Q. Jia, J. Long, X. Wang, Z. Gao, Q. Gu, _Appl. Catal. B_ **2018**, _222_, 35.

[23] L. Cheng, H. Yin, C. Cai, J. Fan, Q. Xiang, _Small_ **2020**, _16_, 2002411.

[24] Y. Li, R. Jin, Y. Xing, J. Li, S. Song, X. Liu, M. Li, R. Jin, _Adv. Energy Mater._ **2016**, _6_, 1601273.

[25] a) Hengpan Yang, Qing Lin, Chao Zhang, Xinyao Yu, Zhong Cheng, Guodong Li, Qi Hu, Xiangzhong Ren, Qianling Zhang, Jianhong Liu, Chuanxin He, _Nat. Commun._ **2020**, _11_, 593; b) J. Chen, H. Li, C. Fan, Q. Meng, Y. Tang, X. Qiu, G. Fu, T. Ma, _Adv. Mater._ **2020**, _32_, 2003134; c) C. M. Zhao, Y. Wang, Z. J. Li, W. X. Chen, Q. Xu, D. S. He, D. S. Xi, Q. H. Zhang, T. W. Yuan, Y. T. Qu, J. Yang, F. Y. Zhou, Z. K. Yang, X. Q. Wang, J. Wang, J. Luo, Y. F. Li, H. H. Duan, Y. Wu, Y. D. Li, _Joule_ **2019**, _3_, 584.

[26] S. Wu, H. Liu, C. Yang, X. Li, Y. Lin, K. Yin, J. Sun, Q. Teng, C. Du, Y. Zhong, _Chem. Eng. J._ **2020**, _392_, 123683.

[27] M. Y. Gao, C. B. Sun, H. Lei, J. R. Zeng, Q. B. Zhang, _Nanoscale_ **2018**, _10_, 17546.

[28] J. Chen, H. Li, C. Fan, Q. Meng, Y. Tang, X. Qiu, G. Fu, T. Ma, _Adv. Mater._ **2020**, _32_, 2003134.

[29] J. Yang, Z. Qiu, C. Zhao, W. Wei, W. Chen, Z. Li, Y. Qu, J. Dong, J. Luo, Z. Li, Y. Wu, _Angew. Chem. Int. Ed._ **2018**, _57_, 14095.

[30] K. Jiang, S. Siahrostami, T. Zheng, Y. Hu, S. Hwang, E. Stavitski, Y. Peng, J. Dynes, M. Gangisetty, D. Su, K. Attenkofer, H. Wang, _Energy Env. Sci_ **2018**, _11_, 893.

[31] T. Zheng, K. Jiang, N. Ta, Y. Hu, J. Zeng, J. Liu, H. Wang, _Joule_ **2019**, _3_, 265.

[32] K. Feng, H. Zhang, J. Gao, J. Xu, Y. Dong, Z. Kang, J. Zhong, _Appl. Phys. Lett._ **2020**, _116_, 191903.

[33] a) C. Sun, H. Zhang, H. Liu, X. Zheng, W. Zou, L. Dong, L. Qi, _Appl. Catal. B_ **2018**, _235_, 66-; b) H Yang, Z Jin, H Hu, Y Bi, G Lu, _Appl. Surf. Sci._ **2018**, _427_, 587.

[34] G. Dong, D. L. Jacobs, L. Zang, C. Wang, _Appl. Catal. B_ **2017**, _218_, 515.

[35] W. Che, W. Cheng, T. Yao, F. Tang, W. Liu, H. Su, Y. Huang, Q. Liu, J. Liu, F. Hu, Z. Pan, Z. Sun, S. Wei, _J. Am. Chem. Soc._ **2017**, _139_, 3021.

[36] a) Z. Lu, C. Li, J. Han, L. Wang, S. Wang, L. Ni, Y. Wang, _Appl. Catal. B_ **2018**, _237_, 919; b) P. Basyach, A. K. Guha, S. Borthakur, L. Kalita, P. Chetia, K. Sonowalab, L. Saikia, _J. Mater. Chem. A_, **2020**, _8_, 12774; c) A. Lewalska-Graczyk, P. Pieta, G. Garbarino, G. Busca, M. Holdynski, G. Kalisz, A. Sroka-Bartnicka, R. Nowakowski, M. Naushad, M. B. Gawande, R. Zbořil, I. S. Pieta, _ACS Sustainable Chem. Eng._ **2020**, _8_, 7244; d) S. Kumar, M. B. Gawande, J. Kopp, S. Kment, R. S. Varma, R. Zbořil, _ChemSusChem_ **2020**, _13_, 5231; e) L. Cheng, H. Yin, C. Cai, J. Fan, Q. Xiang, _Small_ **2020**, _16_, 2002411.

[37] "European Commission Decision 2018/1147 establishing best available techniques for waste treatment, under Directive 2010/75/EU of the European Parliament and of the European Council", **2018**; http://data.europa.eu/eli/dec_impl/2018/1147/oj (accessed April 2021).

[38] L. Cheng, H. Yin, C. Cai, J. Fan, Q. Xiang, *Small* **2020**, *16*, 2002411.

[39] Q. Tay, P. Kanhere, C. F. Ng, S. Chen, S. Chakraborty, A. C. H. Huan, T. C. Sum, R. Ahuja, Z. Chen, *Chem. Mater.* **2015**, *27*, 4930.

[40] H. Yaghoubi, Z. Li, Y. Chen, H. T. Ngo, V. R. Bhethanabotla, B. Joseph, S. Ma, R. Schlaf, A. Takshi, *ACS Catal.* **2015**, *5*, 327.

[41] F. Wang, Y. Wang, Y. Li, X. Cui, Q. Zhang, Z. Xie, H. Liu, Y. Feng, W. Lv, G. Liu, *Dalton Trans.* **2018**, *47*, 6924.

[42] H. Darmstadt, L. Sümmchen, J. M. Ting, U. Roland, S. Kaliaguine, C. Roy, *Carbon* **1997**, *35*, 1581.

[43] I. S. Pieta, A. Rathi, P. Pieta, R. Nowakowski, M. Holdynski, M. Pisarek, A. Kaminska, M. B. Gawande, R. Zboril, *Appl. Catal. B* **2019**, *244*, 272.

[44] M. J. Lázaro, Y. Echegoyen, I. Suelves, J. M. Palacios, R. Moliner, *Appl. Catal. A* **2007**, *329*, 22.

[45] A. Jorio, E. H. Martins Ferreira, M. V. O. Moutinho, F. Stavale, C. A. Achete, R. B. Capaz, *Phys. Status Solidi B* **2010**, *247*, 2980.

[46] B. Quinn, W. Schmidt, K. O'Rourke, R. Hernan, *Chemosphere* **2011**, *84*, 657.

2100176 (12 of 12)